Materials Views
www.MaterialsViews.com

ADVANCED ELECTRONIC MATERIALS
www.advelectronicmat.de

FULL PAPER

Enhancement of Dielectric Properties in Epitaxial Bismuth Ferrite–Bismuth Samarium Ferrite Superlattices

*Ronald Maran, Shintaro Yasui, Eugene Eliseev, Anna Morozovska, Hiroshi Funakubo, Ichiro Takeuchi, and Nagarajan Valanoor**

Artificially layered bismuth ferrite ($BiFeO_3$)/bismuth samarium ferrite $(Bi_{1-x}Sm_x)FeO_3$ superlattices (SLs) are investigated for their dielectric properties. In short-period (5–10 nm) SLs, the stabilization of an incommensurately modulated nanoscale mixture due to a strong interlayer coupling mechanism results in a large dielectric permittivity ($\varepsilon_{33} \approx 170$ at 1 MHz), reduced loss tangent, and increased tunability ($\tau \approx 37\%$) for a samarium concentration range much larger than that for single-layer $(Bi_{1-x}Sm_x)FeO_3$ thin-films. The enhanced dielectric tunability is observed across a large frequency and temperature range. Increasing the thickness of the SL layers reduces the strength of the interlayer coupling, which results in reductions in dielectric permittivity ($\varepsilon_{33} \approx 150$), increases in dielectric loss tangent and decreased tunability ($\tau \approx 14\%$). A phenomenological model confirms that the enhanced dielectric properties, tunability and stabilization of the polar phase to higher Sm^{3+} concentrations over a wide range of temperatures and frequencies in the short period SLs is due to electrostatic coupling. Thus, the epitaxial short-period SLs have significant potential as a highly tunable lead (Pb)-free materials system in low-to-medium frequency applications. Electrostatic coupling effect between polar/non-polar layers in SL structures could thus be a universal method to achieve enhanced dielectric properties.

1. Introduction

Ferroelectric superlattices (SLs) have been demonstrated to have superior, and sometimes even unique properties compared to their single layer thin-film counterparts. The precise level of control made possible by modern thin-film growth techniques has allowed for tailoring of interfaces by tuning either epitaxial strain and/or polarity as well as electronic character.[1–4] The imposed 2D constraint between the interfaces has been exploited in perovskites to induce ferroelectricity,[5–7] enhance electromechanical and dielectric performance,[8–11] and even influence ferroic phase transitions and domain structures.[12–17]

In the same vein, we recently demonstrated successful interface control of a morphotropic phase boundary in 200 nm thick (001) oriented $BiFeO_3/(Bi_{1-x}Sm_x)FeO_3$ (BFO/BSFO) SLs.[18] It was found that the field induced ferroelectric (rhombohedral (R)) → paraelectric (orthorhombic (O)) phase transition driven by Sm^{3+} substitution into the Bi^{3+} site could be controlled by tuning the SL period, although the average composition for all SLs were kept constant. Short period SLs (5 and 10 nm thick individual layers) acted as a single coupled system with strong interlayer polar coupling. Consequently, an incommensurately modulated phase (a nanoscale mixture bridging the Bi-rich rhombohedral and Sm-rich orthorhombic phases) superstructure was found to be stabilized over an increased Sm^{3+} concentration range, as high as 17% Sm^{3+} for the short period SLs. Note that in comparison, in single layer BSFO, 17% Sm^{3+} is already a nonpolar paraelectric. These short period SL films demonstrate saturated ferroelectric hysteresis loops and butterfly-shaped $C_{\varepsilon 33}$–V curves even for the highest Sm^{3+} concentrations in the SLs. This interface coupling is found to weaken with increasing thickness of the multilayer components, in agreement with several other

---

Dr. R. Maran, Prof. N. Valanoor
School of Materials Science and Engineering
The University of New South Wales
Sydney 2052, Australia
E-mail: nagarajan@unsw.edu.au

Dr. S. Yasui
Materials and Structures Laboratory
Tokyo Institute of Technology
4259 Nagatsuta-cho, Midori-ku, Yokohama 226-8502, Japan

Dr. E. Eliseev
Institute for Problems of Materials Science
NAS of Ukraine
Krjijanovskogo 3, 03142 Kyiv, Ukraine

Dr. A. Morozovska
Institute of Physics
NAS of Ukraine
Prospect Nauky 46, 03028 Kyiv, Ukraine

Prof. H. Funakubo
Department of Innovative and Engineered Materials
Tokyo Institute of Technology
4259 Nagatsuta-cho, Midori-ku, Yokohama 226-8502, Japan

Prof. I. Takeuchi
Department of Materials Science and Engineering
University of Maryland
College Park, MD 20742, USA

DOI: 10.1002/aelm.201600170

reports.[4,13,14,19–22] When the individual layer thickness is increased to 50 nm, the thin-film layers decouple fully, reverting broadly back to the single layer BSFO system in terms of polar signature and behavior.

Here, the dielectric nature of these SLs is reported in further detail. We define the SL nomenclature with $[h/h]_m$, with h being the layer thickness in nm, and m being the number of layers of the SL components. We investigate the effects of temperature, periodicity, DC bias and AC frequency on the dielectric permittivity and tunability of overall 200 nm thick (001) oriented BFO/BSFO SLs with $[5/5]_{20}$, $[10/10]_{10}$, and $[50/50]_2$ periods, respectively. By maintaining a fixed total thickness, and symmetrical thicknesses for the two components, each SL has an average composition of $(BFO)_{0.5}/(BSFO)_{0.5}$ in the thickness direction. Therefore, any changes in the observed dielectric behavior can be solely attributed to the changes in the local structure/composition.

It is found that the interlayer coupling of the highly periodic $[5/5]_{20}$ and $[10/10]_{10}$ SLs allows for a high level of control and tailoring of the dielectric character of the multilayer. With increasing Sm^{3+} content, the maximum measured dielectric permittivity continues to monotonically increase from $\varepsilon_{33} \approx 130$ to a maximum of $\varepsilon_{33} \approx 220$ in the $[5/5]_{20}$ SLs, coupled with reduced dielectric loss tangent, tan δ, to ≈0.1@1 MHz. Temperature dependence studies demonstrate that with decreasing temperatures, there is no suppression of the incommensuration phenomenon and hence no sign of the onset of the field-induced O → R phase transition in the dielectric behavior is found. Studies on dielectric tunability demonstrate a marked increase in dielectric tunability (τ) in $[5/5]_{20}$ SLs, with τ as large as ≈37%. This enhanced dielectric tunability remains robust at high temperatures and AC frequencies, between 80–293 K and 10 kHz–1 MHz, respectively. Zero-bias dielectric permittivity measurements further reinforce the robust dielectric behavior at low temperatures, with $[5/5]_{20}$ and $[10/10]_{10}$ SLs showing monotonically increasing ε_{33} up to 17% Sm^{3+} at 80K and 200 K. This suggests artificially layered BFO/BSFO SLs may be ideal for Pb-free applications where frequency and temperature dependent tunability are desirable properties in highly tunable capacitors.

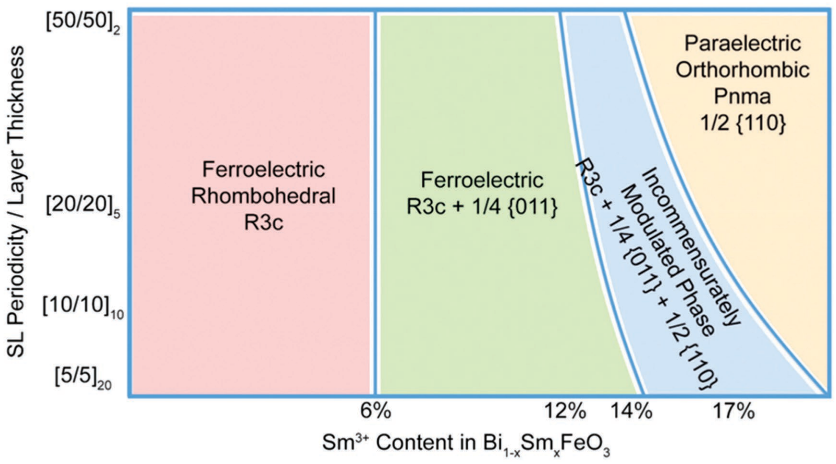

Figure 1. Schematic diagram (abstracted from a previous report[18]) demonstrating the structural evolution of BFO/BSFO SL as a function of increasing Sm^{3+} content, and with SL periodicity at room temperature.

2. Results and Discussion

Figure 1 abstracts the findings of our previous work using a schematic phase diagram at room temperature summarizing the structural features of BFO/BSFO SLs as a function of SL periodicity, and with increasing Sm^{3+} concentration.[18] This is also captured in **Table 1**, which presents a summary of the evolution of structural phases present as a function of increasing Sm^{3+} concentration in 200 nm thick BFO/BSFO SLs, and in single layer BSFO films, based on previous reports.[18,23] Figure 1 and Table 1 are meant to provide a guide to understand how the changes in the structure and composition determine the evolution of the polar (dielectric) behavior, as uncovered in previous work,[18] the gist of which is given below.

For 0%–12% Sm^{3+} concentration both, single-layer BSFO thin-films and the BFO/BSFO SLs exhibit similar behaviors. At Sm^{3+} concentration between 0% and 6%, the ferroelectric *R3c* structure is observed. As further chemical pressure is applied due to increased Sm^{3+} substitution (up to 12%), pockets of an antipolar $PbZrO_3$-like phase begin to emerge, as indicated in X-ray diffraction (XRD) spectra as a ¼{011} superstructure peak. It is beyond 12% Sm^{3+}, where stark distinctions between the behaviors of the short period SLs ($[5/5]_{20}$ and $[10/10]_{10}$) and the longer period ($[50/50]_2$ SL and single-layer BSFO thin-films) appear. The electrostatic coupling between the SL layers

Table 1. Summary of structural phases present in BFO/BSFO SLs and single layer $(Bi_{1-x}Sm_x)FeO_3$ thin-films.[18,23]

Crystallographic features	$[5/5]_{20}$	$[10/10]_{10}$	$[50/50]_2$	Single layer BSFO
Rhombohedral *R3c*	0%–6%	0%–6%	0%–6%	0%–6%
R3c + ¼ {011} superstructure, pockets of antipolar PZO-like phase	6%–12%	6%–12%	6%–12%	6%–12%
Incommensurately modulated phase with coexistence of pockets of *R3c* + ¼ {011} and pockets of orthorhombic cell doubled ½{010} superstructure	12%–17%	12%–17%	12%–14%	12%–14%
Morphotropic phase boundary with increasing orthorhombic cell doubled ½{010} superstructure	N/A	N/A	14%–17%	14%–17%
Only orthorhombic cell doubled phase with ½{010} superstructure	N/A	N/A	>17%	>17%

competes against the chemical pressure, driving the FE part of the phase diagram to higher Sm^{3+} concentrations.

The $[50/50]_2$ SL and single-layer BSFO thin-films exhibit an incommensuration phenomenon, where the polar *R*3*c* + ¼ {011} and orthorhombic nonpolar ½{010} phases coexist for Sm^{3+} concentrations between 12% and 14%. Previous reports[23–26] have demonstrated this region exhibits enhanced dielectric behavior. For Sm^{3+} concentrations beyond this, a nonpolar ½{010} phase emerges between 14% and 17% Sm^{3+}, and eventually becomes the only existing phase beyond 17% Sm^{3+}.

In contrast, the $[5/5]_{20}$ and $[10/10]_{10}$ SLs not only show the incommensurately modulated phase beyond 12% Sm^{3+} concentration, but also the Sm^{3+} compositional range over which this phase is stabilized now extends to well beyond the measured 17% Sm^{3+}. Consequently, the structural transition from polar R → nonpolar O phase does not occur. The objective of the present study thus is to systematically measure the dielectric characteristics of the SLs in as wide a parameter space as possible, and understand how the structural phase distinctions between the various SLs manifest themselves in the measured dielectric responses. This will in turn facilitate the understanding of the important role played by interlayer coupling strengths in SLs and how it can be harnessed to create epitaxial multilayer materials systems with excellent dielectric properties.

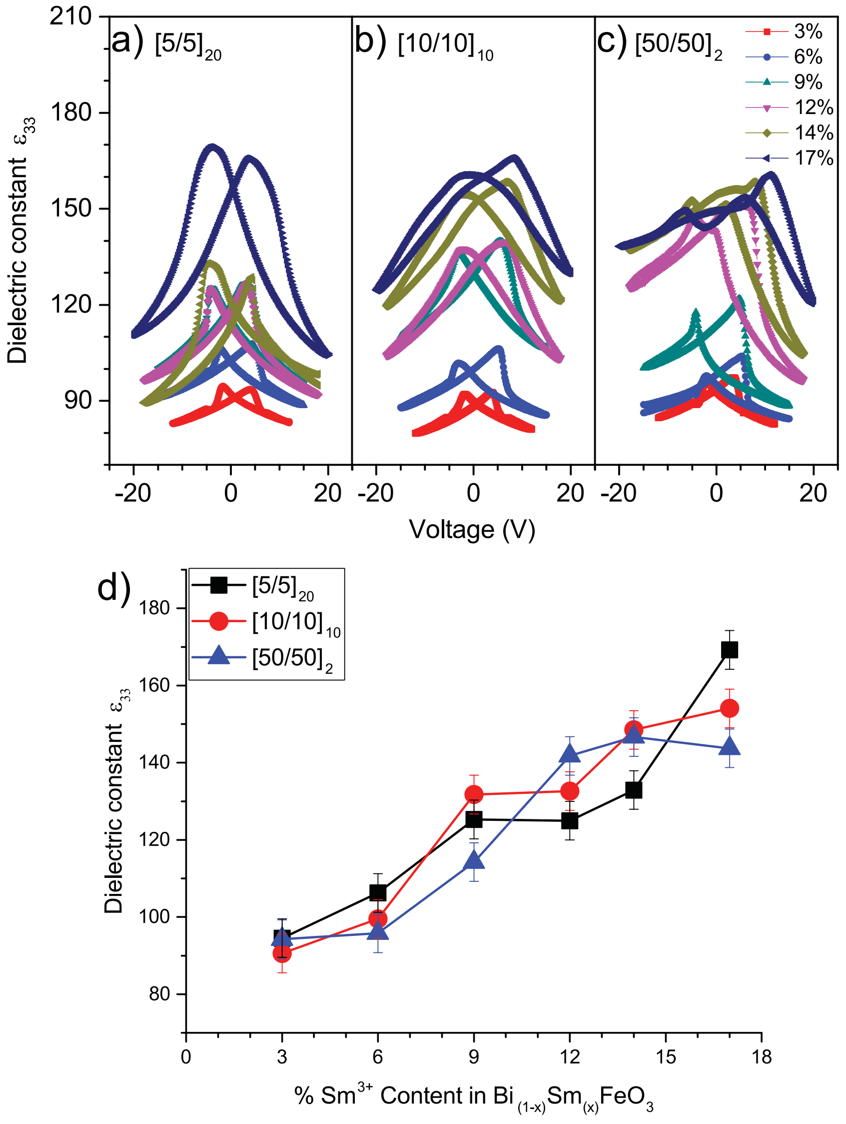

Figure 2. a–c) A comparison of maximum dielectric permittivity (ε_{33})–voltage measurements at a temperature of 200 K with a HP4194A LCR Meter at 1 MHz, demonstrating the evolution in the dielectric permittivity in response to DC bias, and with varying the periodicity of the BFO/BSFO SL between a) $[5/5]_{20}$, b) $[10/10]_{10}$, and c) $[50/50]_2$, respectively. d) Maximum dielectric permittivity (ε_{33}) as a function of composition with varying the SL periodicity. At higher Sm^{3+} content, the $[50/50]_2$ superlattices present quadruple humps, which are characteristic of a double hysteretic loop caused by the polar (R) to nonpolar (O) structural transition. In contrast, the $[5/5]_{20}$ and $[10/10]_{10}$ SLs continue to present increases in the dielectric permittivity with increasing Sm^{3+} content, and do not appear to reach a local maximum. This is consistent with the stabilization of the incommensurately modulated phase in this composition range.

Figure 2 presents a comparison of maximum dielectric permittivity (ε_{33})–voltage measurements acquired at 200 K with a HP4194A LCR Meter at 1 MHz for the $[5/5]_{20}$, (2a) $[10/10]_{10}$ (2b), and $[50/50]_2$ nm (2c) SLs (loss tangent–voltage measurements are found in Supplementary Figure S1, Supporting Information). 200 K was initially chosen in order to minimize dielectric leakage in the BFO/BSFO SLs. We start with the comparison of the peaks in the dielectric (so-called dielectric maxima). For the $[5/5]_{20}$ and $[10/10]_{10}$ SLs, with increasing Sm^{3+} content, the maximum measured dielectric permittivity continues to monotonically increase up to the measured 17% Sm^{3+}, reaching a maximum of $\varepsilon_{33} \approx 170$ and 160, respectively. The measured dielectric loss tangent tan δ is reduced to ≈0.1@1 MHz. This agrees with previous measurements reported for 100 kHz.[18] In contrast, the $[50/50]_2$ SLs exhibit maxima in dielectric permittivity of $\varepsilon_{33} \approx 145$ at 14% Sm^{3+}; beyond this, the maximum ε_{33} begins to decrease, reaching $\varepsilon_{33} \approx 140$ at the maximum measured 17% Sm^{3+}. This also agrees with previous measurements reported at 100 kHz.[18]

In addition to comparing the values, comparing the changes in the shape is also insightful. Note that there is no significant change in the shape of the ε_{33}-*V* curves for the $[5/5]_{20}$ SLs up to the measured 17% Sm^{3+} concentration. However, in the $[10/10]_{10}$ SLs, peak broadening is observed for compositions beyond 12% Sm^{3+}, which can be attributed to the onset of a field induced O ↔ R phase transition. Whilst this appears as a fine shoulder for the [10/10] SL, a clear double hysteretic ε_{33}-*V* loop (with four peaks displaying asymmetry associated with dielectric imprint[40]) is observed for the $[50/50]_2$ system. The changes

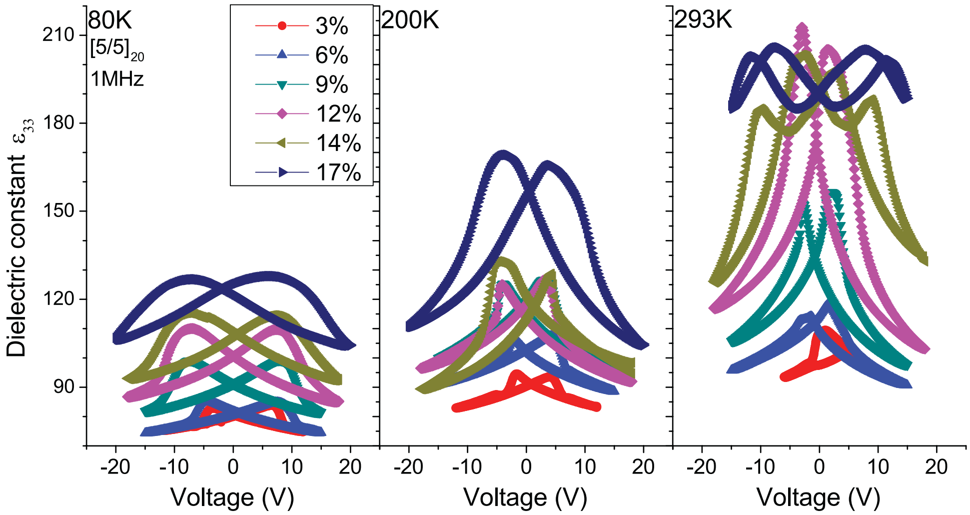

Figure 3. Cold stage ε_{33}–voltage measurements taken 80, 200, and 293 K for the [5/5]$_{20}$ SL at 1 MHz. Note the significantly reduced dielectric permittivity and the absence of a quadruple-humped hysteresis loop with reducing temperature, which suggests that the polar (R) → nonpolar (O) field-induced phase transition is arrested with reducing temperature.

in shape agree with observations in single-layer $Bi_{1-x}Sm_xFeO_3$ thin-films, where the appearance of double-hysteretic butterfly loops are associated with the stabilization of a cell-doubled orthorhombic phase,[27] induced by increases in temperature or by chemical pressure due to Sm^{3+} substitution.[18]

When one compares the remnant (zero DC bias) values, a monotonic increase in the dielectric permittivity (up to 17% Sm^{3+}) is seen in the [5/5]$_{20}$ SL and [10/10]$_{10}$ SL. The [50/50] SL in comparison reaches a maximum remnant value at a composition of 14% Sm^{3+}, and subsequently decreases. This continued increase in the peak dielectric permittivity in the short period SLs (and the contrasting saturation/subsequent decrease in peak dielectric permittivity in the longer period [50/50]$_2$ SL) indicates shifting of the field-induced O ↔ R phase boundary to higher Sm^{3+} concentrations correlated to the introduction of interlayer coupling, confirmed by our previously reported phase diagram[18] and Table 1.

We next examined the temperature response of this shift of the O ↔ R phase transition and stabilization of the $R3c$ + ¼ {011} phase to higher Sm^{3+} concentrations for short period SLs. Our previous report on single layer BSFO thin-films have revealed that an increase in temperature facilitates straddling of the field-induced R → O phase transition, where in $R3c$ + ¼ {011} phase with the antiparallel cation displacements transforms into the cell-doubled orthorhombic phase.[27] That is, effectively with increased temperature, even with a lower Sm^{3+} concentration the materials system is able to undergo the field-induced O ↔ R phase transition, and hence a change in the dielectric response, both, in terms of change of shape of the curve as well as magnitude is expected. Essentially the dielectric response manifests itself first as a peaking of the ε_{33}, and then subsequent peak broadening and quadrupling, as found for the [10/10]$_{10}$ SL in Figure 2.

Conversely, with decreasing temperature the phase stability region for the incommensurately modulated phase should expand, in this particular case, beyond the measured 17% Sm^{3+} in Figure 2, thereby suppressing the O ↔ R phase transition and shifting it to higher Sm^{3+} compositions.

To investigate if our above hypothesis is true, **Figure 3** presents the temperature sensitivity of ε_{33} for the [5/5]$_{20}$ SLs was investigated. In addition to the 200 K measurements, data were acquired at 80 and 293 K. (tangent tan δ–voltage measurements are found in Supplementary Figure S2, Supporting Information). Measurements were also attempted for [10/10]$_{10}$ and [50/50]$_2$ SLs at higher temperatures. However, large leakage currents limited the measurements of the larger period SLs.

The 80 K data are qualitatively similar to the 200 K measurements. There is no observation of the quadruple-humped butterfly curves associated with the onset of the O → R phase transition for the entire Sm^{3+} composition range studied. Thus the low temperature data confirm suppression of the incommensuration phenomenon, and hence the O ↔ R phase transition. In contrast, at 293 K quadruple-humped butterfly shaped loops appear for 14 and 17% Sm^{3+} concentrations. Previous reports have indicated that increases in temperatures in ferroelectric compositions of single layer BSFO thin-films can induce phase transitions between the R → O phases,[18,27] and similar behavior is reported here.

In order to understand the importance of this suppression of the field induced O ↔ R phase transition, we compared the dielectric tunabilities of the [5/5]$_{20}$ nm SLs at various temperatures and compositions. Here we define the dielectric tunability ratio, τ, by

$$\tau = \frac{\varepsilon_{33}(V) - \varepsilon_{33}(0\ V)}{\varepsilon_{33}(0\ V)} \tag{1}$$

where V is the maximum applied DC bias.

Figure 4 plots a comparison of a) dielectric tunability ratio τ (±5%) versus Sm^{3+} concentration for each SL periodicity at 1 MHz for a fixed temperature of 200K, b) tunability versus AC frequency of [5/5]$_{20}$ SLs, and c) tunability versus composition for the three different temperatures for the [5/5]$_{20}$ SL at 1 MHz. The [5/5]$_{20}$ SL is presented here due to difficulty in acquiring suitable ε_{33}-V data at 293 K for the [10/10]$_{10}$ and [50/50]$_2$ SLs.

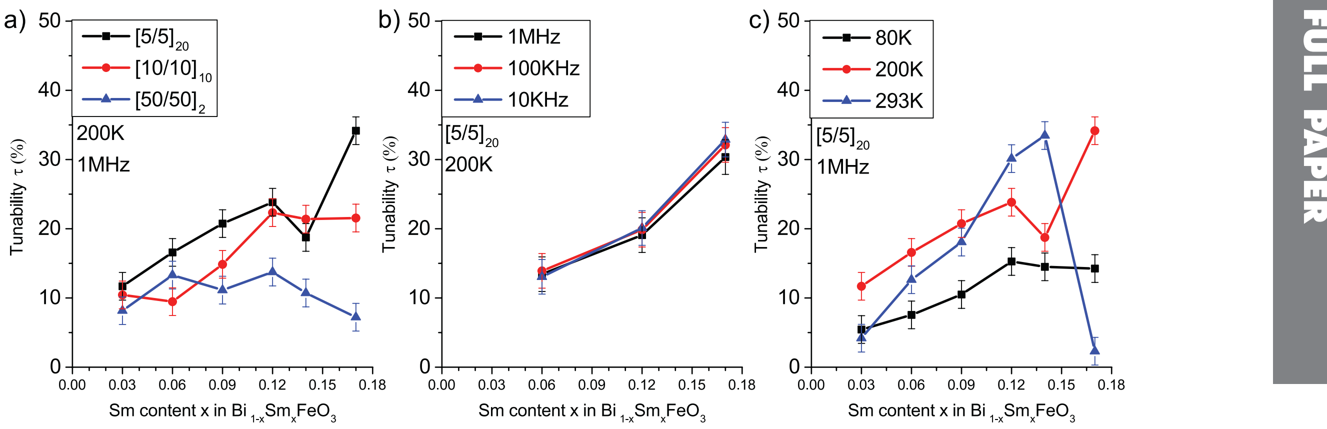

Figure 4. Comparison of a) dielectric tunability as a function of Sm^{3+} concentration for each SL periodicity at 1 MHz and 200 K. b) Tunability versus Sm^{3+} concentration for three different AC frequencies for the $[5/5]_{20}$ SL at 200 K, and c) tunability as a function of Sm^{3+} concentration for three different temperatures for the $[5/5]_{20}$ SLs at fixed 1 MHz frequency.

In Figure 4a, we can now see the effect of the SL periodicity (i.e., the effect of increasing the strength of the interlayer interactions) on the dielectric tunability. The tunability of the $[5/5]_{20}$ SL continues to monotonically increase up to 17% Sm^{3+} content, reaching a maximum tunability of ≈34.16%. The $[10/10]_{10}$ SLs reach a maximum tunability at 12% Sm^{3+} concentration (≈22.33%) and then saturates (within error) until 17% Sm^{3+}. In comparison, the $[50/50]_2$ SLs display a maximum τ of ≈13.75% at 12% Sm^{3+}, and then decreases up to the measured 17% Sm^{3+} concentration to ≈7.21%. These trends agree with the ε_{33}-V data presented in Figure 2, where the value of the difference between $\varepsilon_{33}(0\ \text{V})$ and $\varepsilon_{33}(V)$ decreases at the measured compositions between 12% and 17% Sm^{3+} concentration.

In Figure 4b, the temperature and the SL period ($[5/5]_{20}$) is fixed, and the effects of AC frequency modulation on the tunability is compared. All AC frequencies display an upward trend in τ with increasing Sm^{3+} concentration—correlating with previous ε_{33}-V sweep measurements for this sample subset. The $[5/5]_{20}$ SLs display similar trends in τ regardless of AC frequency used. The maximum observed τ varies between ≈30.36% and 32.9% (17% Sm^{3+}) which compare favorably to other potential lead-free ceramics for tunable dielectrics such as $BaSrTiO_3$ and (Ba,Ca)(Ti,Zr)O_3 in addition to previous reports on BFO.[28–30] The previous ε_{33}-V data from Figures 1 and 2 suggest that the monotonically increasing τ is linked to the suppression of the field induced O → R phase transition, and stabilization of the incommensurately modulated phase. This hints the maximum τ value may be realized by tuning the temperature or increasing the Sm^{3+} content beyond the measured 17% Sm^{3+}.

The temperature sensitivity is shown in Figure 4c, where the AC frequency and SL periodicity are fixed at 1 MHz and $[5/5]_{20}$, respectively. For a given temperature, by tuning the composition such that it promotes the field-induced O → R phase transition (through the formation of the incommensurately modulated phase), we realize a markedly high τ. For example, this is realized at ≈17% (τ of 34.15%) at 200 K; for 293 K it is restricted to 12%–14%. Recall that for these two temperatures, these high concentrations of Sm^{3+} represent regions of the incommensurately modulated phase. The ferroelectric compositions of the BSFO layers exhibit phase transitions induced by both the electric-field application[18] and at high temperatures[27] between the R → O phases,[18,27] and consequently the difference between $\varepsilon_{33}(V)$ and $\varepsilon_{33}(0\ \text{V})$ and thus τ decreases. In comparison, the effects of the suppression of the field-induced O → R phase transition (and hence absence of the incommensurately modulated phase) driven by the reduction in temperature is demonstrated well at 80 K. In the case of the 80 K measurements the τ value remains only in the range of ≈14%–15% for the concentration range of 12%–17% Sm^{3+}. This suggests that a pathway to achieve high τ is to achieve conditions such that the incommensurately modulated phase phase is stabilized and also sheds light on the maximum layer thicknesses that can be employed to engineer SLs with enhanced electromechanical properties for such systems.

In order to obtain a clearer picture of the frequency dependence of the dielectric properties of SLs, ε_{33}-f, and ε_{33}-V measurements were carried out at both zero-bias and under DC-bias application with varying AC frequencies.

Figure 5 compares the frequency dependence of ε_{33}-V and loss tangent sweeps in $[5/5]_{20}$ SLs for three different frequencies (10 KHz, 100 KHz, and 1 MHz, respectively) at 200 K. To highlight the clear trends, we discuss only data obtained for selected key structural compositions of 6% Sm^{3+} (*R*3*c*), 12% Sm^{3+} (*R*3*c* + ¼ <011> superstructure), and 17% Sm^{3+} (incommensurately modulated phase), although frequency sweeps were acquired for the entire composition spread. First, we observe that at for all compositions, there is a frequency driven dielectric stiffening of ε_{33} (particularly notable at dielectric maxima) in the measured frequency range of 10 kHz to 1 MHz (for an applied bias of −3.5 V). This stiffening may be attributed to a ferroelectric (FE) lattice instability causing a shift in the strength of the soft modes at the measured frequency range.[31,32] There is also a large variation in the dielectric loss with AC frequency for the *R*3*c* phase; this is a trend previously observed for single layer *R*3*c* BSFO thin-films.[23] For 12% Sm^{3+} content, the $[5/5]_{20}$ SL has a much reduced loss tangent (up to threefold compared with the 6% Sm^{3+} concentration) at 10 kHz. There is also a marked improvement in the magnitude of the dielectric maximum up from ≈140 at 10 kHz to ≈125 at 1 MHz. At 17% Sm^{3+} where the $[5/5]_{20}$ SL structurally is in the incommensurately modulated

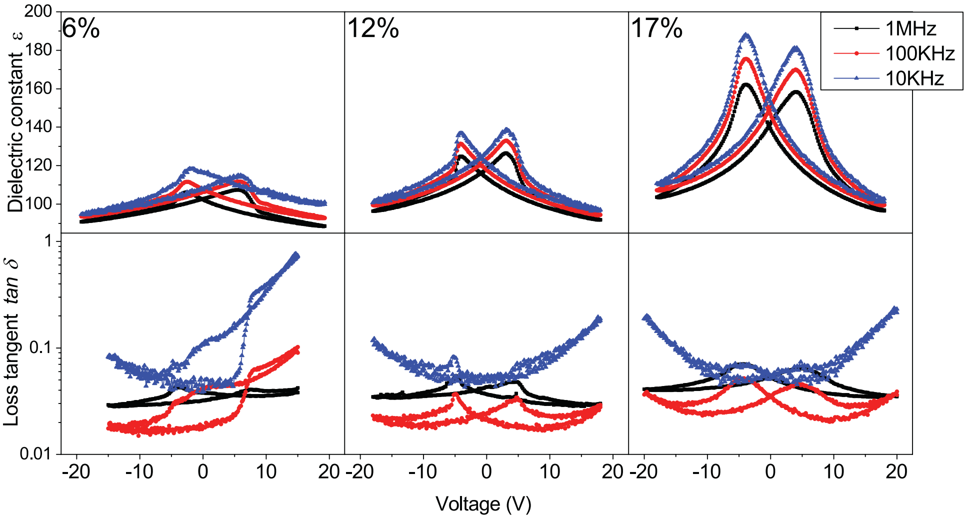

Figure 5. Comparison of frequency dependence on ε_{33}–voltage and loss tangents in $[5/5]_{20}$ SLs at 200 K for selected structural compositions of 6% Sm^{3+} ($R3c$), 12% Sm^{3+} ($R3c$ + ¼ {011} superstructure), and 17% Sm^{3+} (incommensurately modulated phase).

phase; there is a dramatic increase in the dielectric maximum going up to the range of ≈190 (for 10 KHz) and ≈160 (for 1 MHz). This is in agreement with the previous finding[18] that highlights the key role played by the incommensurately modulated phase in improving electromechanical behavior. However, note that the measured capacitance (i.e., effectively the dielectric permittivity) is far more sensitive to the applied frequency in case of the 17% as compared to the 6%. For example the 6% Sm^{3+} sample shows a ≈10% variation which increases to ≈20% for the 17% case. Surprisingly this occurs with little change in loss tangent to the $R3c$ + ¼ {011} superstructure phase.

Figure 6 plots the AC frequency dependence of the zero bias dielectric permittivity ε_{33}(0 V) as a function of the Sm^{3+} content in the $[5/5]_{20}$, $[10/10]_{10}$, and $[50/50]_2$ SLs at temperatures of 80 and 200 K, respectively. To simplify the data, selected compositions of 6%, 12%, and 17% Sm^{3+}, at frequencies of 1 kHz, 10 kHz, 100 kHz, 1 MHz, and 10 MHz are presented. Full datasets of all measured compositions and AC frequencies are provided in the Supplementary Figure S3 of the Supporting Information.

In the $[5/5]_{20}$ and $[10/10]_{10}$ SLs, the ε_{33} (0 V) monotonically increases within the measured composition range up to 17% Sm^{3+} irrespective of the measurement frequency, at both 80 and 200 K. This trend agrees with data obtained from the ε_{33}-V studies reported previously,[18] and in Figure 3, where the maximum ε_{33} monotonically increases with increasing Sm^{3+} substitution up to 17% Sm^{3+}.

For the $[50/50]_2$ SL, its behavior parallels the other short period SLs up to 12% Sm^{3+} at 80 K, displaying a monotonic increase in dielectric permittivity. The ε_{33}(0 V) then stabilizes—maintaining a value of ≈130 at 12%, 14%, and 17% Sm^{3+} content. In contrast when the measurement temperature increases to 200 K—a saturation at 12% Sm^{3+} and then subsequent reduction in ε_{33}(0 V) at 14% and 17% Sm^{3+} is observed. This is in agreement with the ε_{33}-V loop shown for 200 K in Figure 2 which, at zero-bias applied DC shows an identical saturation of dielectric permittivity at 12% Sm^{3+}, and subsequent decrease at 14% and 17% Sm^{3+} content. Thus the $[50/50]_2$ SLs exhibit similar trends to single layer BSFO thin-films.[32,33]

In order to understand the importance of the incommensurately modulated phase on the polarization, modelling based on Landau–Ginsburg–Devonshire (LGD) thermodynamic theory[18,34,35] was performed. The nonlinear LGD approach gives an excellent description of the polar and dielectric behavior of graded multilayers.[36] Full mathematical details are provided in the Supplementary Figure S4 of the Supporting Information. Let us start with phenomenological Landau–Khalatnikov equation for polarizations in each of the layers

$$\Gamma\frac{\mathrm{d}P^{(1)}}{\mathrm{d}t}+\alpha_1(T)P^{(1)}+\beta\left(P^{(1)}\right)^3-g\frac{\mathrm{d}^2P^{(1)}}{\mathrm{d}z^2}=E^{(1)}\quad\text{for}\quad 0\le z\le h_1 \tag{2a}$$

$$\Gamma\frac{\mathrm{d}P^{(2)}}{\mathrm{d}t}+\alpha_2(T)P^{(2)}+\beta\left(P^{(2)}\right)^3-g\frac{\mathrm{d}^2P^{(2)}}{\mathrm{d}z^2}=E^{(2)}\quad\text{for}\quad -h_2\le z<0 \tag{2b}$$

Hereinafter coefficients $\alpha_{1,2}$ depend on temperature T and Sm^{3+} content x in one of the layers, nonlinearity coefficient β is regarded the same. The electrostatic boundary conditions, which take into account the presence of the surface screening length (i.e., free charges) at the interfaces between the layers, are

$$\left(D^{(1)}-D^{(2)}+\varepsilon_0\frac{\phi}{\lambda}\right)\Bigg|_{z=0}=0,\quad \phi\big|_{z=+0}-\phi\big|_{z=-0}=0 \tag{3}$$

Here $D^{(i)}=\varepsilon_{bi}E^{(i)}+P^{(i)}$ and λ is the surface screening length. Note that the boundary conditions are that the first derivative of the polarization with respect thickness at the interfaces is continuous (otherwise it will lead up to the bound charges abrupt at the interface)

$$\frac{\mathrm{d}}{\mathrm{d}z}P_3^{(1)}(-h_1)=\frac{\mathrm{d}}{\mathrm{d}z}P_3^{(2)}(-h_1),\ \frac{\mathrm{d}}{\mathrm{d}z}P_3^{(1)}(0)$$
$$=\frac{\mathrm{d}}{\mathrm{d}z}P_3^{(2)}(0),\ \frac{\mathrm{d}}{\mathrm{d}z}P_3^{(1)}(-h_1)=\frac{\mathrm{d}}{\mathrm{d}z}P_3^{(2)}(-h_1) \tag{4}$$

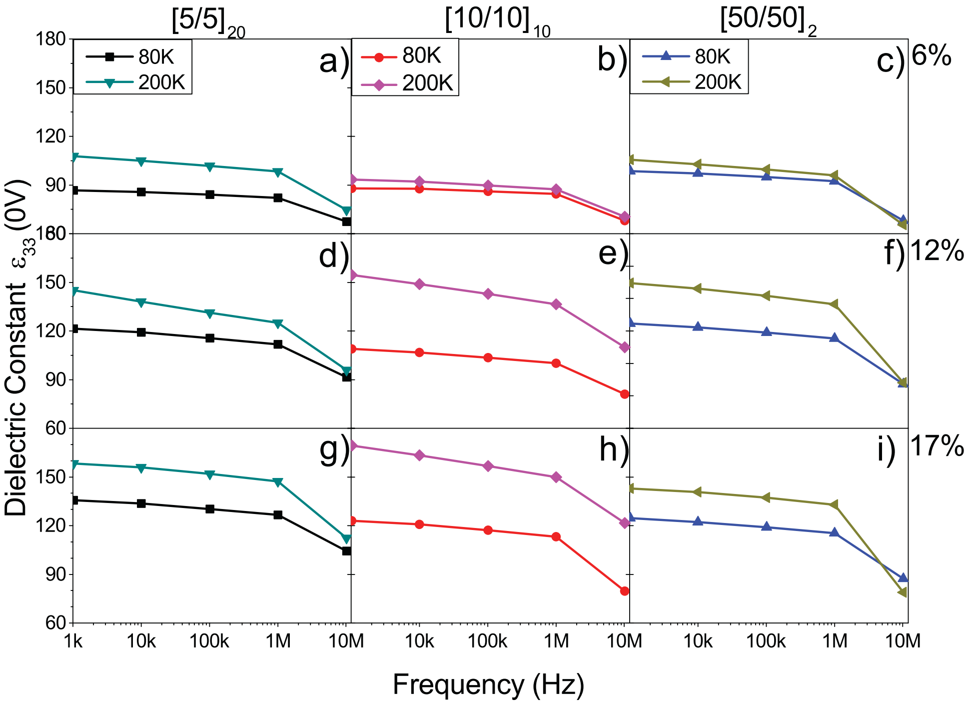

Figure 6. Variance in ε_{33} based on Sm^{3+} concentration and SL periodicity at selected frequencies of 1 kHz, 10 kHz, 100 kHz, 1 MHz, and 10 MHz at compositions of 6% (a,d,g), 12% (b,e,h), and 17% (c,f,i) Sm^{3+} concentrations. For 80 K a maximum ε_{33} is observed at 17% in all SLs. In contrast at 200 K, a saturation and subsequent reduction in ε_{33} in $[50/50]_2$ SLs is observed as Sm^{3+} concentration approaches the compositional range of the field-induced polar (R) → nonpolar (O) phase transition.

The dielectric permittivity is calculated using a serial scheme, i.e., $\varepsilon_{33}=\frac{\varepsilon_{33}^{(1)}\varepsilon_{33}^{(2)}}{\varepsilon_{33}^{(1)}+\varepsilon_{33}^{(2)}}$, where $\varepsilon_{33}^{(1)}=\frac{dP_3^{(1)}}{\varepsilon_0 dE}$ and $\varepsilon_{33}^{(2)}=\frac{dP_3^{(2)}}{\varepsilon_0 dE}$. The dielectric tunability is then given as $\tau=\frac{\varepsilon_{33}(\delta V)-\varepsilon_{33}(0)}{\varepsilon_{33}(0)}$, where δV is the applied voltage on the single layer (SL). This value can be small for the linear susceptibility calculations, but can take moderate numbers for the calculations of nonlinear tunability.

A sketch of the calculated geometry is shown in the **Figure 7**a. Fitting to the experiment is shown in the Figure 7b,c. When doing the fitting we regard that the parameters λ and x_0 can vary within the ranges indicated in the **Table 2**. Material parameters for bulk ferroelectric $Bi_{1-x}Sm_xFeO_3$ were collected.[37–40] Note that λ is different for 200 and 300 K, because the surface conductivity changes strongly with temperature.

Figure 7b,c predicts that the peak of dielectric properties, especially tunability (associated with a rather diffuse phase transition) moves to higher Sm concentration with multilayer period decrease. The peak moves to higher Sm composition values for 5 and 10 nm and then simply reverts to the single layer film value for a 50 nm multilayer period. This trend can be explained by the fact that the thinner SL $(Bi_{1-x}Sm_x)FeO_3$ layers act as high-*k* interlayers with or without additional screening with the surface length λ when the amount of Sm^{3+} substitution is sufficient to induce the incommensurately modulated phase. Thus the spontaneous polarization of ultrathin BFO layers is screened better than the large period

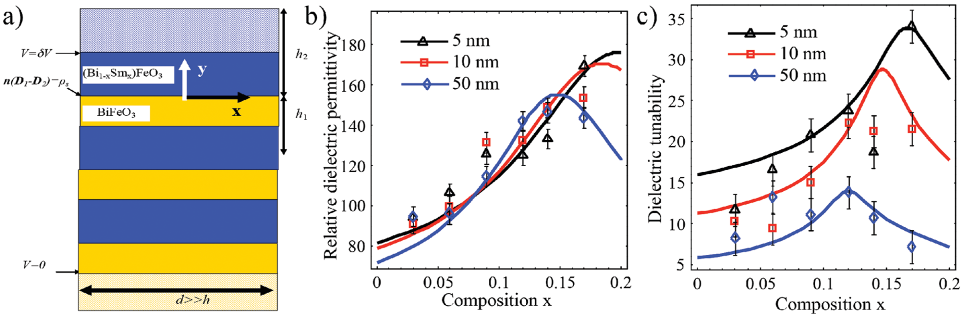

Figure 7. a) Schematic of the SL, b) relative dielectric permittivity, and c) tunability**.** Symbols are experimental data at 200 K, solid curves are theoretical fitting for the parameters listed in Table 2.

Table 2. Material parameters for bulk ferroelectrics at room temperature 293 °K.

Coefficient	$BiFeO_3$	$Bi_{1-x}Sm_xFeO_3$
ε_b	6	6
α_T [$\times 10^5$ C^{-2} mJ K^{-1}]	0.81	0.81
T_C [K]	$T_C = 1100$	$T_C(x) = T_C(e - \exp(x/x_0))/(e-1)$ that gives $\approx T_C(1-(x/x_0))$ at $x \approx x_0$, where x_0 varied in the range 0.17–0.12 to fit the observed value of the critical concentrations
β [$\times 10^8$ C^{-4} m^5 J]	10.9	10.9
λ [nm]	(0–5) nm	The range corresponds to the cross-over from half-metal to band-gap semiconductor interface to fit the experiment

SL where the stray fields penetrate into the BSFO layer via the interface.

3. Conclusion

In summary, low-temperature frequency dependent dielectric property characteristics of 200 nm BFO/BSFO SLs have been investigated. We have experimentally confirmed that a high degree of control over the dielectric properties in this system. Large dielectric tunability ratios >30%, as well as low temperature suppression of the incommensurately modulated nanoscale mixture phase has been observed. ε_{33}(0 V) is constant over a large frequency range of 10 kHz–1 MHz. Compared with single layer BSFO thin-films, these SLs exhibit frequency enhanced dielectric permittivity ε_{33} for Sm^{3+} compositions up to 17% and improved dielectric loss tangents. The resulting ability to tune the dielectric properties of this artificially layered multiferroic material can open the door to low frequency (sub-GHz) applications.

4. Experimental Section

Combinatorial pulsed laser deposition was used to fabricate composition spreads of 200 nm [$BiFeO_3$/($Bi_{1-x}Sm_x$)FeO_3] SLs on an $SrRuO_3$ buffer layer. For each film, a composition spread has a gradient composition from $x = 0$ to $x = 0.25$ across an 8 mm length of the substrate. Ceramic targets of $Bi_{1.1}FeO_3$ (Kurt J. Lesker) and $SmFeO_3$ (Praxair) were ablated with a KrF Excimer Laser ($\lambda = 248$ nm, Thin-Film Star). Temperatures of 630 °C, 100 mTorr O_2 partial pressure, laser fluency of 0.8 J cm^{-2}, and laser pulse frequency of 5 Hz were used to grow the $SrRuO_3$ bottom electrode to a total thickness of 50 nm. BFO/BSFO SLs were then grown at 590 °C, 25 mTorr oxygen partial pressure, 0.8 J cm^{-2} Laser Fluency, and 40 Hz Laser pulse frequency. The thickness of each layer was varied between 5 and 50 nm per layer, and all samples were grown to the total thickness of 200 nm. The experimental schematic of composition spread deposition has been previously reported.[18] The composition variation across the spread multilayers were probed using an electron probe (JEOL JXA-8900, Japan), with accuracy of ±1% at each measurement point. Electrical characterization was facilitated through the deposition and patterning via lift-off process of 50 × 50 × 0.1 µm Pd top electrodes, in addition to physically masked circular 100 × 0.1 and 200 × 0.1 µm Pt electrodes grown via electron beam deposition. Detailed XRD measurements of the BFO/BSFO SLs have been previously reported.[18] Dielectric properties were measured using an LCR Meter (HP 4194A) using an AC signal of 80 mV and frequencies ranging from 10 kHz to 1 MHz and 100 Hz to 20 MHz for maximum dielectric permittivity-voltage (ε_{33}-V) and maximum dielectric permittivity-frequency (ε_{33}-f) measurements, respectively, in a custom cold-stage measurement station set to temperatures of 80, 200, and 293 K, at a chamber base pressure of ≈5×10^{-5} Torr. Note that for purposes of context, we compare the maximum dielectric permittivity (ε_{33}) in all figures, computed by a standard parallel plate capacitor model.

Supporting Information

Supporting Information is available from the Wiley Online Library or from the author.

Acknowledgements

The manuscript was written through contributions of all authors. All authors have given approval to the final version of the manuscript. The research at UNSW was supported by an ARC Linkage Project. A.N.M. and E.E acknowledges the Center for Nanophase Materials Sciences, under Project No. CNMS2016-061 and the National Academy of Sciences of Ukraine (Grant No. 07-06-15). R.M. and V.N. acknowledge funding and support from Thales Australia. S.Y. acknowledges for Grant-in-Aid for Young Scientists (Start-up: 25889025), JSPS. H.F. acknowledges financial support from Kakenhi (No. 15H04121). The authors thank Dr. Rama Vasudevan for his careful reading and comments on the manuscript.

Received: April 26, 2016
Revised: May 24, 2016
Published online:

---

[1] H. Jang, D. Felker, C. Bark, Y. Wang, M. Niranjan, C. Nelson, Y. Zhang, D. Su, C. Folkman, S. Baek, S. Lee, K. Janicka, Y. Zhu, X. Pan, D. Fong, E. Tsymbal, M. Rzchowski, C. Eom, *Science* **2011**, *331*, 886.
[2] a) A. Ohtomo, D. Muller, J. Grazul, H. Hwang, *Nature* **2002**, *419*, 378; b) A. Ohtomo, H. Hwang, *Nature* **2004**, *427*, 423.
[3] J. Wu, J. Wang, D. Xiao, J. Zhu, *ACS Appl. Mater. Interfaces* **2011**, *3*, 2504.
[4] J. Wu, J. Wang, D. Xiao, J. Zhu, *ACS Appl. Mater. Interfaces* **2012**, *4*, 1182.
[5] E. Bousquet, M. Dawber, N. Stucki, C. Lichtensteiger, P. Hermet, S. Gariglio, J. Triscone, P. Ghosez, *Nature* **2008**, *452*, 732.
[6] H. Lee, H. Christen, M. Chisholm, C. Rouleau, D. Lowndes, *Nature* **2005**, *433*, 395.
[7] K. Johnston, X. Huang, J. Neaton, K. Rabe, *Phys. Rev. B* **2005**, *71*, 100103.
[8] M. Osada, T. Sasaki, *Adv. Mater.* **2012**, *24*, 210.
[9] A. Roytburd, S. Zhong, S. Alpay, *Appl. Phys. Lett.* **2005**, *87*, 092092.
[10] M. Dawber, N. Stucki, C. Lichtensteiger, S. Gariglio, P. Ghosez, J. Triscone, *Adv. Mater.* **2007**, *19*, 4153.
[11] M. Dawber, C. Lichtensteiger, M. Cantoni, M. Veithen, P. Ghosez, K. Johnston, K. Rabe, J. Triscone, *Phys. Rev. Lett.* **2005**, *95*, 177601.

[12] J. Sinsheimer, S. Callori, B. Bein, Y. Benkara, J. Daley, J. Coraor, D. Su, P. Stephens, M. Dawber, *Phys. Rev. Lett.* **2012**, *109*, 067061.
[13] N. Lemée, I. Infante, C. Hubault, A. Boulle, N. Blanc, N. Boudet, V. Demange, M. Karkut, *ACS Appl. Mater. Interfaces* **2015**, *7*, 19906.
[14] P. Zubko, N. Jecklin, A. Torres-Pardo, P. Aguado-Puente, A. Gloter, C. Lichtensteiger, J. Junquera, O. Stéphan, J. Triscone, *Nano Lett.* **2012**, *12*, 2846.
[15] C. Lichtensteiger, S. Fernandez-Pena, C. Weymann, P. Zubko, J. Triscone, *Nano Lett.* **2014**, *14*, 4205.
[16] G. Pacchioni, S. Valeri, *Oxide Ultrathin Films*, John Wiley & Sons, **2012**.
[17] P. Aguado-Puente, P. García-Fernández, J. Junquera, *Phys. Rev. Lett.* **2011**, *107*, 217601.
[18] R. Maran, S. Yasui, E. Eliseev, M. Glinchuk, A. Morozovska, H. Funakubo, I. Takeuchi, V. Nagarajan, *Phys. Rev. B* **2014**, *90*, 245131.
[19] V. Cooper, K. Johnston, K. Rabe, *Phys. Rev. B* **2007**, *76*, 020103.
[20] S. Li, J. Eastman, J. Vetrone, R. Newnham, L. Cross, *Philos. Mag. B* **1997**, *76*, 47.
[21] I. Misirlioglu, M. Kesim, S. Alpay, *Appl. Phys. Lett.* **2014**, *104*, 022906.
[22] P. Wu, X. Ma, Y. Li, V. Gopalan, L. Chen, *Appl. Phys. Lett.* **2012**, *100*, 092905.
[23] D. Kan, L. Pálová, V. Anbusathaiah, C. Cheng, S. Fujino, V. Nagarajan, K. Rabe, I. Takeuchi, *Adv. Funct. Mater.* **2010**, *20*, 1108.
[24] C. Cheng, D. Kan, S. Lim, W. McKenzie, P. Munroe, L. Salamanca-Riba, R. Withers, I. Takeuchi, V. Nagarajan, *Phys. Rev. B* **2009**, *80*, 014109.
[25] C. Cheng, D. Kan, V. Anbusathaiah, I. Takeuchi, V. Nagarajan, *Appl. Phys. Lett.* **2010**, *97*, 212905.
[26] S. Emery, C. Cheng, D. Kan, F. Rueckert, S. Alpay, V. Nagarajan, I. Takeuchi, B. Wells, *Appl. Phys. Lett.* **2010**, *97*, 152902.
[27] C. Cheng, A. Borisevich, D. Kan, I. Takeuchi, V. Nagarajan, *Chem. Mater.* **2010**, *22*, 2588.
[28] X. Tang, K. Chew, J. Wang, H. Chan, *Appl. Phys. Lett.* **2004**, *85*, 991.
[29] M. Cole, W. Nothwang, C. Hubbard, E. Ngo, M. Ervin, *J. Appl. Phys.* **2003**, *93*, 9218.
[30] J. Nath, D. Ghosh, J. Maria, A. Kingon, W. Fathelbab, P. Franzon, M. Steer, *Trans. Microwave Theory Tech.* **2005**, *53*, 2707.
[31] S. Kamba, D. Nuzhnyy, M. Savinov, J. Šebek, J. Petzelt, J. Prokleška, R. Haumont, J. Kreisel, *Phys. Rev. B* **2007**, *75*, 024403.
[32] H. Uchida, R. Ueno, H. Funakubo, S. Koda, *J. Appl. Phys.* **2006**, *100*, 4106.
[33] H. Uchida, R. Ueno, H. Nakaki, H. Funakubo, S. Koda, *Jpn. J. Appl. Phys.* **2005**, *44*, L561.
[34] V. Stephanovich, I. Luk'yanchuk, M. Karkut, *Phys. Rev. Lett.* **2005**, *94*, 047601.
[35] A. Borisevich, E. Eliseev, A. Morozovska, C. Cheng, J. Lin, Y. Chu, D. Kan, I. Takeuchi, V. Nagarajan, S. Kalinin, *Nat. Commun.* **2012**, *3*, 775.
[36] M. Okatan, A. Roytburd, J. Mantese, S. Alpay, *J. Appl. Phys.* **2009**, *105*, 114106.
[37] J. Zhang, Y. Li, Y. Wang, Z. Liu, L. Chen, Y. Chu, F. Zavaliche, R. Ramesh, *J. Appl. Phys.* **2007**, *101*, 114105.
[38] V. Lemanov, *Phys. Solid State* **1997**, *39*, 628.
[39] G. Catalan, J. Scott, *Adv. Mater.* **2009**, *21*, 2463.
[40] M. Okatan, S. Alpay, *Appl. Phys. Lett.* **2009**, *95*, 092092.